Bitemporal Spatial Autocorrelation Matrix for Change Detection in Multispectral Imagery: A Case Study on the Drying of a Lake in Southern Italy

Giovanni Piccolo[1 2], Cinzia Sada[1]

[1]Università degli Studi di Padova - Physics & Astronomy Department “G. Galilei”, Via Marzolo 8, 35131 Padova, Italy
[2]Engineering Ingegneria Informatica S.p.A., Piazzale dell’Agricoltura 24, 00144 Roma, Italy

Keywords: Change Detection, Spatial Autocorrelation, BSAC Matrix, Symmetry Index, Sentinel-2, NDWI

Abstract

Multispectral satellite imagery provides an essential source of information for monitoring environmental transformations, yet robust unsupervised change detection remains challenging due to radiometric variability and seasonal dynamics. At the same time, supervised approaches based on Deep Learning are often constrained by the need for computationally expensive accelerated hardware and the limited availability of high-quality annotated datasets. This work introduces a framework based on the Bitemporal Spatial Autocorrelation (BSAC) matrix, that rather than relying on pixel-wise spectral differencing or data-intensive Deep Learning models, it is designed to quantify structural changes by evaluating the symmetry properties of the spatial autocorrelation across multiple spatial lags. Three complementary metrics are derived from the BSAC representation: a binary change/no-change trigger (χ) that identifies structural discontinuities, an asymmetry magnitude (Δ) that measures the intensity of change, and a normalized Symmetry Index (SI) obtained via singular value decomposition to characterize the geometric coherence of the correlation structure. The methodology is applied to Sentinel-2 imagery of Lake Fanaco (Sicily, Italy), which experienced severe desiccation during the 2024 drought. Experiments conducted using NDWI and NDVI confirm the index-agnostic nature of the framework, capturing both hydrological contraction and vegetation stress. Comparison with an unsupervised K-means segmentation baseline shows strong spatial agreement in identifying the affected areas. Thanks to its unsupervised formulation and near-linear computational complexity, the BSAC framework represents a scalable and interpretable approach for operational change monitoring in Earth observation.

1. Introduction

Monitoring surface changes through satellite remote sensing is a central task in Earth Observation (EO), enabling the characterization of environmental processes driven by climatic variability and anthropogenic pressure. The capability to monitor phenomena such as water depletion, vegetation loss, and land use transformation relies on the robustness of Change Detection (CD) algorithms. With the increasing availability of high-revisit multispectral constellations such as Sentinel-2 (Drusch et al., 2012), the bottleneck has shifted from data acquisition to the development of automated and unsupervised analytical frameworks capable of discriminating genuine environmental change from variability induced by illumination differences, atmospheric conditions, and residual preprocessing artifacts.

Historically, the literature on unsupervised change detection has been dominated by algebraic and statistical approaches. Techniques such as Change Vector Analysis (CVA), image differencing, and ratioing operations (Singh, 1989, Coppin et al., 2004, Malila, 1980) operate on the assumption that changes manifest as statistically significant departures in spectral feature space. While computationally efficient, these methods often depend on heuristic decision rules (e.g., threshold selection) and may be sensitive to residual atmospheric effects, illumination/view-geometry differences, imperfect co-registration, and seasonal phenological variability, which can reduce transferability across sensors, seasons, and biomes (Bruzzone and Prieto, 2000, Lu and Moran, 2004, Radke et al., 2005).

Recently explored methodologies designed to overcome these traditional bottlenecks have driven the development of more complex CD algorithms, with a strong focus on Deep Learning (DL) paradigms and, in particular, for Convolutional Neural Networks (CNNs) and Siamese architectures (Daudt et al., 2018, Bai et al., 2023). Although recent surveys map this rapid expansion, they also expose persistent vulnerabilities. In particular, the operational deployment of DL models is often inhibited by the scarcity of large, high-quality, consistently annotated bitemporal datasets (limited training labels), cross-domain shifts, and heterogeneous data sources (Shafique et al., 2022, Parelius, 2023, Cheng et al., 2024, Jiang et al., 2024). Furthermore, the computational burden of deep feature extraction can be prohibitive for large-area or near-real-time monitoring (Ding et al., 2025). Although a parallel line of research has explored weakly supervised or alternative unsupervised paradigms (such as object-based analysis and statistical transformations as kernel-PCA) to increase robustness without massive datasets (Hussain et al., 2013, Radke et al., 2005, Wu et al., 2022), balancing contextual sensitivity with algorithmic simplicity remains a challenge. Consequently, there is a distinct need for unsupervised methods that can offer the structural awareness of complex models while maintaining the computational lightness of algebraic operators.

To overcome these limitations, this study proposes an unsupervised approach that exploits the spatial autocorrelation structure of spectral indices as a quantitative descriptor of change. The fundamental premise of this work is that if a geographical area undergoes limited or no physical changes between two observation times, its spatio-temporal pattern remains constant i.e., the local spatial autocorrelation structure of the pixels is preserved over time (Moran, 1950, Cressie, 1993). On the other hand, significant morphological changes disrupt this local coherence, inducing anisotropy in the spatial correlation field. We formalize this concept through the construction of the Bitemporal Spatial Autocorrelation (BSAC) Matrix, a descriptor that encodes the covariance between spatial neighborhoods across two acquisition times (i.e., the pre- and post-event states).

By analyzing the algebraic and geometric properties of the BSAC matrix, we derive a hierarchical suite of index-agnostic metrics: a binary stability trigger (χ), an asymmetry magnitude score (Δ), and a normalized Symmetry Index (SI) computed via Singular Value Decomposition (SVD). Together, these indicators quantify the presence, intensity, and morphological regularity of environmental change as a function of the breaking of symmetry in the autocorrelation field. This approach bridges the gap between purely visual and purely categorical change representations, enabling both robust detection and precise quantification of environmental transformations. Unlike conventional or deep learning-based approaches, it requires no training data and integrates spatial context directly into the change metric, making it highly suitable for regional-scale monitoring such as surface drying.

2. Methodology

2.1 Study Area and Data Preprocessing

The study area of the proposed framework focuses on Lake Fanaco (37.66°N, 13.55°E), a strategic artificial reservoir located in central Sicily (Italy). During 2024, this area became a focal point of a severe regional drought, emblematic of the broader climate-induced water crisis that affected southern Europe, culminating in the declaration of a regional emergency state (Euronews, 2024). The reservoir experienced a drastic reduction in water volume, leading to near-total desiccation by the end of the summer, which triggered emergency water supply protocols for surrounding municipalities.

To capture this extreme transition, two Sentinel-2 Level-2A multispectral images were selected as representative temporal snapshots: a pre-event image acquired in January 2024 (high water level) and a post-event image from October 2024 (near-complete desiccation), as shown in Figure 1.

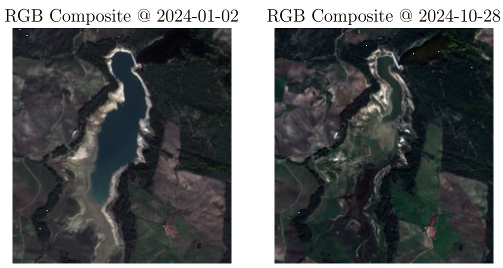

Figure 1. True-color (RGB) Sentinel-2 composite of Fanaco Lake (Italy) acquired in January (left) and October 2024 (right).

While the true-color composites provide a qualitative overview of the lake's contrasting hydrological states, the Normalized Difference Water Index (NDWI) was computed to quantitatively enhance the visibility of surface water dynamics. Specifically, to isolate surface water features, the NDWI (McFeeters, 1996) was calculated using the Green ($B3$, central wavelenght 560 nm) and Near-Infrared ($B8$, central wavelenght 842 nm) spectral bands of the Sentinel-2 sensor (Gascon et al., 2017):

$$NDWI = \frac{\rho_{Green} - \rho_{NIR}}{\rho_{Green} + \rho_{NIR}} \tag{1}$$

where ρ represents the surface reflectance. Positive NDWI values typically correspond to water surfaces, whereas lower or negative values indicate vegetation or bare soil, allowing a clear differentiation between flooded and dried areas (see Figure 2).

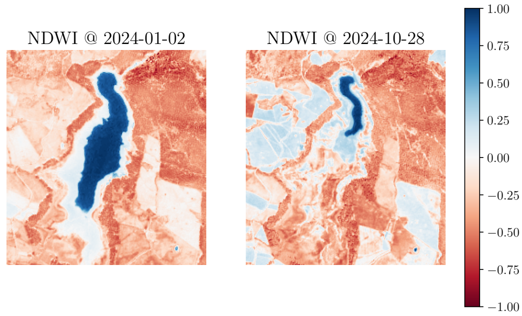

Figure 2. NDWI maps derived from Sentinel-2 imagery of Fanaco Lake for January (left) and October 2024 (right).

To demonstrate the versatility and index-agnostic nature of the proposed framework, a secondary analysis was designed using the Normalized Difference Vegetation Index (NDVI). While NDWI captures the direct contraction of the water surface, NDVI is primarily designed to measure photosynthetic activity, representing vegetation health and allowing the assessment of temporal phenological dynamics (Tucker, 1979). NDVI was derived using the Red ($B4$, central wavelenght 665 nm) and NIR bands ($B8$):

$$NDVI = \frac{\rho_{NIR} - \rho_{Red}}{\rho_{NIR} + \rho_{Red}} \tag{2}$$

Applying the BSAC framework to this suboptimal index serves as a methodological stress test to evaluate the generalizability of the algorithm across multiple indices and scenarios. This dual validation approach confirms the structural robustness of the method. The bitemporal NDVI maps used for this secondary analysis are presented in Figure 3.

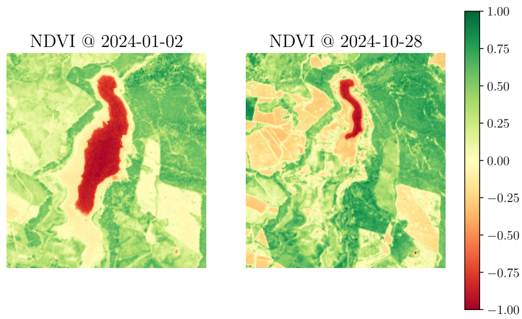

Figure 3. NDVI maps derived from Sentinel-2 imagery of Fanaco Lake for January (left) and October 2024 (right).

Sentinel-2 multispectral optical data were accessed and processed through a openEO process graph via the Copernicus Data Space Ecosystem backend (Schramm et al., 2021). This approach ensures full reproducibility of the data cube generation. The retrieved data consist of Bottom-Of-Atmosphere

(BOA) surface reflectance generated by the official ESA Sen2Cor processing chain, which applies radiometric calibration, atmospheric correction, terrain correction, and geometric co-registration (Louis et al., 2019, Gascon et al., 2017). This rigorous preprocessing strategy ensures that the measured spectral variations are exclusively attributable to genuine physical surface changes rather than atmospheric residuals or sensor-induced artifacts.

To guarantee high-quality observations, image selection was restricted to acquisitions with a scene-level cloud cover of less than 10%. To preserve the original radiometric integrity of the scene, no additional histogram matching or normalization was applied post-retrieval.

2.2 Bitemporal Spatial Autocorrelation Matrix (BSAC)

To quantify the structural coherence of surface changes between two observation times t_1 and t_2, we introduce the Bitemporal Spatial Autocorrelation Matrix $\rho \in \mathbb{R}^{S\times S}$. This descriptor captures the joint spatial and temporal dependencies of a spectral index z across a set of increasing spatial offsets $\{1, \ldots, S\}$.

Let $N = H \times W$ denote the total number of pixels within the analyzed spatial data of height H and width W at a given band. We define $z_{t_1}, z_{t_2} \in \mathbb{R}^N$ as the flattened vectors of the chosen multispectral index (e.g., NDWI) acquired respectively at t_1 and t_2. The spatial context is encoded by applying a set of spatial weight matrices $\mathcal{W} = \{W_1, W_2, \ldots, W_S\}$ to the flattened image vectors, where each matrix W_l captures the neighborhood relationships at a specific spatial lag l. To model the topological adjacency on the regular image grid, we adopt a Queen's case contiguity criterion extended to higher-order lags. Formally, letting (x_i, y_i) and (x_j, y_j) be the two-dimensional spatial coordinates of pixels i and j respectively, the binary entry $w_{ij}^{(l)}$ of the weight matrix W_l is defined using the Chebyshev distance:

$$w_{ij}^{(l)} = \begin{cases} 1, & \text{if } \max(|x_i - x_j|, |y_i - y_j|) = l \\ 0, & \text{otherwise} \end{cases} \tag{3}$$

Geometrically, this definition generates discrete, concentric square boundaries around each pixel, allowing the analysis to probe spatial textures at specific scales (e.g., $l = 1$ captures immediate adjacency, while $l = 5$ captures higher-range context). Instead, from a computational perspective, each W_l is instantiated as a sparse matrix to ensure memory efficiency and it is row-standardized (i.e., each non-zero row is normalized to sum to 1). This seeks to avoid scale effects caused by varying neighbor counts, which is especially necessary for pixels situated near the region of interest boundaries or adjacent to masked pixels.

To quantify surface changes we define a bitemporal spatial autocorrelation (BSAC) matrix $\rho(l, k)$ that captures both spatial and temporal dependencies of a spectral index at time t_1 (lag l) and at time t_2 (lag k):

$$\rho(l, k) = \frac{\mathrm{Cov}(W_l z_{t_1}, W_k z_{t_2})}{\sqrt{\mathrm{Var}(W_l z_{t_1}) \cdot \mathrm{Var}(W_k z_{t_2})}} \tag{4}$$

where $\mathrm{Cov}(\cdot, \cdot)$ denotes spatial covariance. The denominator in the BSAC formulation serves as a normalization factor, bounding each entry $\rho(l, k) \in [-1, 1]$. Consequently, each element $\rho(l, k)$ of the matrix expresses the normalized spatial cross-correlation between a neighborhood of order l at time t_1 (pre-event image) and a neighborhood of order k at time t_2 (post-event image).

In a temporally stable scenario, this matrix is expected to be symmetric and diagonally dominant ($\rho(l, k) \approx \rho(k, l)$). On the other hand, significant morphological changes (e.g., a shoreline retreat or desiccation) disrupt this symmetry, as the spatial correlation at time t_2 no longer mirrors the spatial dependencies at time t_1.

2.3 Change Quantification Metrics

The BSAC matrix captures the multi-scale structural evolution of the analyzed scene within the selected multispectral index. To systematically decode this high-dimensional algebraic structure into actionable indicators, we formulate a hierarchical analysis protocol. This ”decision cascade” consists of three interconnected metrics: a binary stability trigger (χ), an asymmetry magnitude score (Δ), and a morphological Symmetry Index (SI). In the first place, χ determines if the spatio-temporal dependence structure is compatible with a stable environment. If $\chi = 0$, then the scene is structurally invariant. On the other hand, if the data describe a bitemporal change event (and thus $\chi = 1$), we proceed to compute Δ (to quantify the global energy of the asymmetry) and SI (to characterize the geometric regularity and directionality of the distortion).

2.3.1 Structural Stability Trigger (χ) The first level of analysis acts as a binary classifier for temporal continuity. We define an indicator $\chi \in \{0, 1\}$ that tests the BSAC matrix for two fundamental properties expected in a temporally invariant landscape: algebraic symmetry (time-reversibility of spatial dependence) and diagonal dominance (decay of correlation with distance). Operationally, χ provides a binary distinction between symmetric (no-change) and asymmetric (change) configurations:

$$\chi = \begin{cases} 0, & \text{if } ||\rho - \rho^\top||_F < \varepsilon \text{ and } \rho_{ll} \geq \rho_{lk} \ \forall l \neq k \\ 1, & \text{otherwise} \end{cases} \tag{5}$$

where $|| \cdot ||_F$ denotes the Frobenius norm and ε represents a positive tolerance threshold. In the context of real-world remote sensing data, ε serves as an empirical buffer to account for the radiometric and environmental variability between multi-temporal acquisitions, such as differences in solar illumination, atmospheric conditions, or seasonal background noise.

2.3.2 Asymmetry Magnitude (Δ) After the change detection ($\chi = 1$), the overall intensity of the physical alteration is quantified by Δ. This metric measures the magnitude of asymmetry, computed as the Euclidean norm of the difference between the forward ($t_1 \to t_2$) and backward ($t_2 \to t_1$) cross-correlations:

$$\Delta = \sqrt{\sum_{l=1}^{S} \sum_{k=1}^{S} (\rho(l, k) - \rho(k, l))^2} \tag{6}$$

https://doi.org/10.5194/isprs-archives-XLIX-B3-2026-643-2026

From a physical point of view, Δ encapsulates the ”energy” of the symmetry breaking. High values of Δ indicate that the spatial configuration at t_2 constitutes a newly formed topological arrangement (e.g., the emergence of a high-contrast dry boundary within a previously homogeneous water body).

2.3.3 Geometrical Symmetry Index (SI) While Δ provides an absolute scalar magnitude of the structural change, it remains an unbounded metric whose absolute value is inherently tied to the overall variance of the analyzed data. To provide a standardized and scale-independent quantification of the matrix asymmetry, we introduce the Symmetry Index (SI), derived directly from the geometric properties of the matrix in the lag-space.

To compute this index, we derive the optimal reflection axis directly from the geometric properties of the matrix. Let $\rho = U\Sigma V^\top$ be the SVD decomposition of the BSAC matrix, and let θ^* denote the dominant orientation associated with the first singular vector pair (u_1, v_1). The matrix is then evaluated for reflective symmetry across this empirically derived axis.

Let Ω be the set of valid coordinates (i, j) in the matrix domain, and let (r_i, r_j) denote the exact reflection of point (i, j) across the axis θ^*. The Symmetry Index is formulated as:

$$SI = 1 - \sqrt{\frac{1}{E_{max}} \sum_{(i,j)\in\Omega} \Big(\rho(i,j) - \rho(r_i, r_j)\Big)^2} \qquad (7)$$

where $E_{max} = 4N_{valid}$ is the maximum symmetry error. Specifically, N_{valid} counts the total number of valid index pairs in the domain Ω (i.e., the number of matrix cells that have a valid reflected counterpart across the axis θ^*). Since the matrix entries ρ represent normalized spatial correlations strictly bounded in $[-1, 1]$, the maximum possible squared difference between any point and its reflection is $(1 - (-1))^2 = 4$. Multiplying this extreme limit by N_{valid} yields the absolute upper bound for the asymmetry.

The square root introduces a non-linear scaling that makes the index highly sensitive to early structural degradation. While the function’s steep gradient near zero error ensures that even minor alterations trigger a decrease in the metric, this does not compromise its robustness. Because the index measures topological coherence rather than raw pixel values, it strictly responds to genuine morphological shifts, effectively preventing false positive detections in structurally stable scenes.

Consequently, an $SI > 0.90$ reflects a highly isotropic coherence (characteristic of structurally stable environments). Intermediate values (e.g., $SI \approx 0.50$) already denote morphological distortions, as they indicate a substantial fraction of the absolute maximum theoretical error. Finally, $SI \to 0$ represents a complete spatial reorganization or total breakdown of the correlation patterns, describing fundamentally two completely different scenes.

By providing a normalized metric bounded between 0 and 1, SI enables robust comparisons of structural degradation across different scenarios or spectral indices.

3. Results and Discussion

3.1 BSAC Metrics Analysis

The proposed BSAC framework was applied to the bitemporal Sentinel-2 acquisitions of Lake Fanaco to quantify the structural degradation induced by the 2024 drought. The analysis was conducted independently on the NDWI and NDVI spectral features to evaluate the index-agnostic capability of the algorithm. For both indices, the structural stability trigger immediately flagged the binary change detection index as true ($\chi = 1$), confirming a statistically significant rupture in the spatial coherence of the landscape.

The spatial autocorrelation analysis was computed up to a maximum spatial lag of $S = 7$ pixels. Given the 10 m Ground Sampling Distance of the input data, this translates to a physical inspection radius of approximately 70 m. This parameter was selected based on a preliminary sensitivity analysis evaluating the trade-off between feature extraction and computational complexity. Specifically, the analysis revealed that the change metrics reach an informational plateau at $S = 7$. Beyond this threshold, the change detection parameters almost stabilize. Consequently, incorporating further lags meant increasing computing time without providing additional value. In addition, the selected scale fully captures the characteristic correlation length of the morphological transition, while effectively filtering out background environmental noise originating from the surrounding terrestrial environment.

Visual representations of the BSAC matrices provide an intuitive understanding of this structural shift. As illustrated in Figure 4, the alteration of the water body translates into an asymmetric 3D representation of the matrix in the lag space.

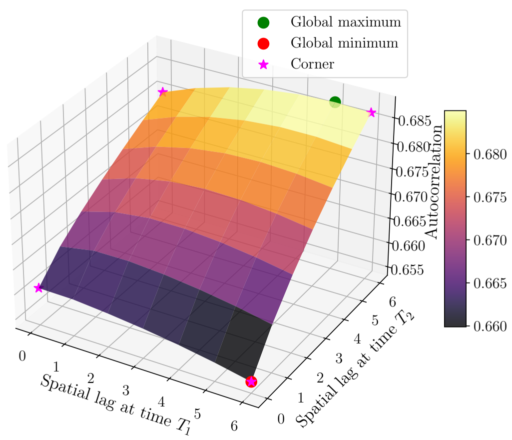

Figure 4. 3D representation of the BSAC matrix derived from NDWI data showing the global extrema and spatial lag interactions between the two dates.

The two-dimensional top view of the same matrix (Figure 5) highlights this asymmetry more clearly, with the SVD axis and the opposing max–min lines visually illustrating the directional imbalance introduced by the surface contraction. The diagonal symmetry expected in stable conditions is disrupted, with the SVD-derived axis diverging by 6.5° from the global max–min direction. The secondary axes display angular deviations of 2.1° and 87.9°, respectively, confirming that the correlation structure departs from isotropy and that spatial dependencies differ between the two acquisition times.

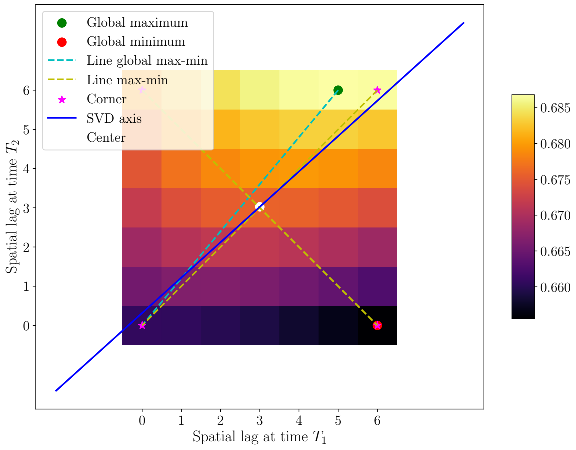

Figure 5. Top-down view of the BSAC matrix derived from NDWI data highlighting the SVD axis and global max-min line, evidencing asymmetry.

Quantitatively, the NDWI analysis yielded an asymmetry magnitude of $\Delta = 0.104$ and a Symmetry Index of $SI = 0.55$, indicating a large spatial distortion. This specific case study describes a ”concentric” morphological retraction: the lake shrank drastically, fundamentally altering the spatial lag relationships, yet it maintained a continuous, coherent central body rather than shattering into random, disconnected noise.

The secondary analysis applied to the NDVI demonstrated the versatility of the framework, yielding a higher magnitude of asymmetry ($\Delta = 0.218$) and a $SI = 0.62$, shown in Figure 6. The higher value of Δ is physically consistent with the widespread nature of the drought. While the NDWI captures high-contrast localized changes predominantly at the retreating water-land boundary, the NDVI responds to broader ecological stress. Alongside the shrinking lake, the severe drought also degraded the surrounding vegetation and agricultural fields. Consequently, the spatial correlation pattern of the NDVI experienced a greater magnitude of change (Δ) across the entire region of interest.

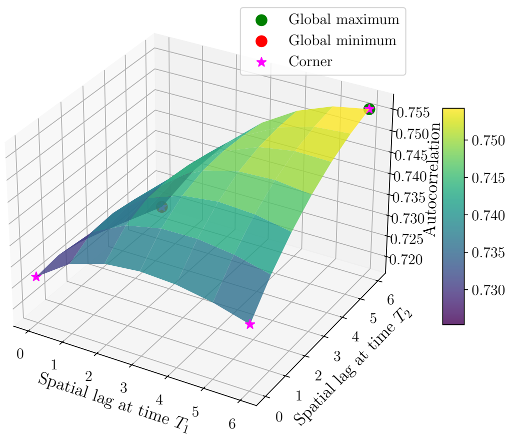

Figure 6. 3D representation of the BSAC matrix derived from NDVI data showing the global extrema and spatial lag interactions between the two dates

3.2 Unsupervised Spectral Segmentation Ground Truth and Quantitative Validation

In order to contextualize BSAC metrics within the physical dynamics of the water-to-bare-soil transition and provide a quantitative accuracy assessment, an unsupervised segmentation benchmark was established. A standard K-means clustering algorithm (with $k = 2$) was applied to the bitemporal NDWI distributions to generate a binary water/non-water mask for both acquisition dates. The differential analysis of these masks reveals a catastrophic physical contraction of the reservoir, with approximately 81.49% of the initial water extent vanishing between January and October 2024 (Figure 7). This massive areal loss provides the physical baseline and ground truth for our analysis.

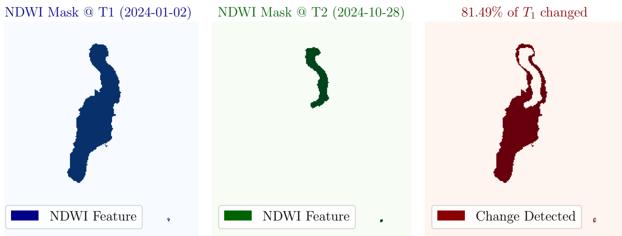

Figure 7. Unsupervised change detection baseline generated via K-means clustering ($k = 2$) on NDWI features. The analysis quantifies a massive surface contraction, with 81.49% of the initial water extent vanishing between January and October 2024.

While the BSAC framework operates primarily as a global, scene-level descriptor of change detection instead of a pixel classificator, we conducted a preliminary analysis to extract a pixel-wise change map. To achieve this, the global asymmetry detected in the lag-space was projected back into the geographic domain. Conceptually, we first identify the dominant spatial lag in $\{1, \ldots, S\}$, defined as the specific scale at which the asymmetry between the BSAC matrix and its transpose is maximized. The spatial weight matrix corresponding to this critical lag is then applied to the absolute difference of the spectral indices to extract a neighborhood-weighted context. Then, we produce an ”anomaly score” for each pixel defined as the element-wise product of the original absolute temporal difference and this spatial context. This composite product is subsequently normalized, effectively translating the lag-space asymmetry computed into a localized, context-aware change probability. By applying an adaptive percentile threshold (dynamically modulated by the global matrix asymmetry) and standard morphological filtering to these local scores, we generated a binary BSAC-derived change map and compared it directly against the K-means ground truth. The quantitative evaluation demonstrated excellent spatial alignment: the BSAC projection achieved an Overall Accuracy (OA) of 98.10% and a robust F1-score of 0.819. Furthermore, the Kappa coefficient reached 0.809, indicating an optimal agreement with the reference map, while maintaining a remarkably low False Positive Rate (8.59%).

These metrics confirm that the geometric asymmetry captured by the BSAC matrix is not only a statistical indicator, but a robust feature that can be successfully translated into accurate spatial boundaries.

3.3 Computational Complexity and Scalability

From an operational perspective, the framework demonstrates high computational efficiency. A naive dense implementation of the spatial weight matrices needed to evaluate the cross-correlation requires $\mathcal{O}(S \cdot N^2)$ memory, which is computationally prohibitive for high-resolution satellite imagery (where $N = H \times W$ is the total number of valid pixels and S the maximum spatial lags). To ensure operational scalability, the proposed BSAC framework relies on two core algorithmic optimizations. First, the spatial weight matrices W_l are strictly instantiated as sparse data structures, reducing the space complexity to $\mathcal{O}(S \cdot N \cdot d)$, where d is the average number of valid neighbors per pixel. Second, the spatially lagged vectors are pre-computed and cached to avoid redundant sparse matrix-vector multiplications, bounding the overall time complexity of the matrix population phase to $\mathcal{O}(S^2 \cdot N \cdot d)$. Because the computational cost scales linearly with the spatial domain N and quadratically with the maximum lag S, the algorithm efficiently processes standard regional subsets (e.g., 10^6 pixels for a $100\,\mathrm{km}^2$ area at $10\,\mathrm{m}$ GSD) without prohibitive memory or processing bottlenecks. By maintaining S within empirically optimal bounds, the framework ensures high operational throughput on standard commercial hardware.

4. Conclusions and Future Work

This study introduced a novel spatial-structural framework for bitemporal change detection, shifting the analytical focus from discrete pixel-wise classification to the evaluation of global topological coherence. By constructing the Bitemporal Spatial Autocorrelation (BSAC) matrix, the proposed approach successfully quantifies the geometric asymmetry between temporal layers across multiple spatial lags. The index-agnostic nature of the framework was validated by monitoring the severe desiccation of Lake Fanaco, Italy, using different spectral indices (NDWI and NDVI). This result confirmed the robustness and broad applicability of the approach across a wide range of potential environmental monitoring scenarios. Unlike traditional threshold-based methods, which are highly susceptible to radiometric inconsistencies and atmospheric noise, or Deep Learning architectures that demand extensive annotated datasets (and expensive hardware for training and inference), the BSAC framework operates in a fully unsupervised manner. Since, by construction, the computational complexity scales linearly with the spatial extent (for any given lag configuration), this framework provides a highly efficient environment that could be advantageous for automated monitoring pipelines where ground-truth training data is scarce, unavailable, or too costly to generate.

The primary operational limitation of the proposed methodology lies in its spatial aggregation at the scene-level. Because the BSAC framework computes a global descriptor of asymmetry rather than acting as a pixel-wise classifier, it does not natively generate a discrete change map for direct Geographic Information System (GIS) integration. Furthermore, the nature of the derived change metrics at this stage (i.e., the asymmetry magnitude Δ and the Symmetry Index SI) requires contextualization, posing potential interpretative challenges.

Future work will address these spatial and interpretative limitations through a systematic sensitivity analysis of the framework parameters, particularly the optimal spatial lag and the stability of the noise tolerance across different environmental contexts. Further research will also investigate methods to project the lag-space asymmetry back into the geographic domain, enabling spatially explicit representations of structural change.

Data and Code Availability

The Sentinel-2 Level-2A products used in this study are publicly available through the Copernicus Data Space Ecosystem. To support reproducibility, the preprocessed `NetCDF` dataset and the openEO process graph used for data retrieval are available from the corresponding author upon reasonable request. The custom code used for the analysis is currently under active development as part of an ongoing project and is therefore not publicly available at this stage.

References

Bai, T., Wang, L., Yin, D., Sun, K., Chen, Y., Li, W., Li, D., 2023. Deep learning for change detection in remote sensing: a review. *Geo-spatial Information Science*, 26(3), 262–288.

Bruzzone, L., Prieto, D. F., 2000. Automatic analysis of the difference image for unsupervised change detection. *IEEE Transactions on Geoscience and Remote Sensing*, 38(3), 1171–1182.

Cheng, G., Huang, Y., Li, X., Lyu, S., Xu, Z., Zhao, H., Zhao, Q., Xiang, S., 2024. Change Detection Methods for Remote Sensing in the Last Decade: A Comprehensive Review. *Remote Sensing*, 16(13), 2355.

Coppin, P., Jonckheere, I., Nackaerts, K., Muys, B., Lambin, E., 2004. Digital change detection methods in ecosystem monitoring: a review. *Remote Sensing of Environment*, 93(1-2), 165–183.

Cressie, N. A. C., 1993. *Statistics for Spatial Data*. Wiley.

Daudt, R. C., Le Saux, B., Boulch, A., 2018. Fully Convolutional Siamese Networks for Change Detection. *arXiv preprint arXiv:1810.08462*.

Ding, L., Hong, D., Zhao, M., Chen, H., Li, C., Deng, J., Yokoya, N., Bruzzone, L., Chanussot, J., 2025. A Survey of Sample-Efficient Deep Learning for Change Detection in Remote Sensing: Tasks, strategies, and challenges. *IEEE Geoscience and Remote Sensing Magazine*, 13(3), 164-189. http://dx.doi.org/10.1109/MGRS.2025.3533605.

Drusch, M., Del Bello, U., Carlier, S., Colin, O., Fernandez, V., Gascon, F., Hoersch, B., Isola, C., Laberinti, P., Martimort, P., Meygret, A., Spoto, F., Sy, O., Marchese, F., Bargellini, P., 2012. Sentinel-2: ESA’s Optical High-Resolution Mission for GMES Operational Services. *Remote Sensing of Environment*, 120, 25–36.

Euronews, 2024. State of emergency declared in sicily due to drought. Euronews (online). Available at: `https://www.euronews.com/2024/03/01/state-of-emergency-declared-in-sicily-due-to-drought`. Accessed: March 2026.

Gascon, F., Bouzinac, C., Thépaut, O., Jung, M., Francesconi, B., Louis, J., Lonjou, V., Lafrance, B., Massera, S., Gaudel-Vacaresse, A., Languille, F., Alhammoud, B., Viallefont, F., Pflug, B., Bieniarz, J., Clerc, S., Pessiot, L., Trémas, T., Cadau, E., De Bonis, R., Isola, C., Martimort, P., Fernandez, V., 2017. Copernicus Sentinel-2A Calibration and Products Validation Status. *Remote Sensing*, 9, 584.

Hussain, M., Chen, D., Cheng, A., Wei, H., Stanley, D., 2013. Change detection from remotely sensed images: From pixel-based to object-based approaches. *ISPRS Journal of photogrammetry and remote sensing*, 80, 91–106.

Jiang, W., Sun, Y., Lei, L., Kuang, G., Ji, K., 2024. Change detection of multisource remote sensing images: a review. *International Journal of Digital Earth*, 17(1).

Louis, J., Pflug, B., Main-Knorn, M., Debaecker, V., Mueller-Wilm, U., Iannone, R. Q., Giuseppe Cadau, E., Boccia, V., Gascon, F., 2019. Sentinel-2 Global Surface Reflectance Level-2a Product Generated with Sen2Cor. *IGARSS 2019 - 2019 IEEE International Geoscience and Remote Sensing Symposium*, 8522–8525.

Lu, Mausel, B., Moran, 2004. Change detection techniques. *International Journal of Remote Sensing*, 25(12), 2365–2401. https://doi.org/10.1080/0143116031000139863.

Malila, W. A., 1980. Change vector analysis: an approach for detecting forest changes with Landsat. 326–335.

McFeeters, S. K., 1996. The use of the Normalized Difference Water Index (NDWI) in the delineation of open water features. *International journal of remote sensing*, 17(7), 1425–1432.

Moran, P. A. P., 1950. Notes on continuous stochastic phenomena. *Biometrika*, 37(1-2), 17–23.

Parelius, E. J., 2023. A Review of Deep-Learning Methods for Change Detection in Multispectral Remote Sensing Images. *Remote Sensing*, 15(8), 2092.

Radke, R. J., Andra, S., Al-Kofahi, O., Roysam, B., 2005. Image change detection algorithms: a systematic survey. *IEEE Transactions on Image Processing*, 14(3), 294–307.

Schramm, M., Pebesma, E., Milenković, M., Foresta, L., Dries, J., Jacob, A., Wagner, W., Mohr, M., Neteler, M., Kadunc, M. et al., 2021. The openEO API–Harmonising the Use of Earth Observation Cloud Services Using Virtual Data Cube Functionalities. *Remote Sensing*, 13(6), 1125.

Shafique, A., Cao, G., Khan, Z., Asad, M., Aslam, M., 2022. Deep Learning-Based Change Detection in Remote Sensing Images: A Review. *Remote Sensing*, 14(4), 871.

Singh, A., 1989. Review Article Digital change detection techniques using remotely-sensed data. *International Journal of Remote Sensing*, 10(6), 989–1003.

Tucker, C. J., 1979. Red and photographic infrared linear combinations for monitoring vegetation. *Remote sensing of Environment*, 8(2), 127–150.

Wu, C., Chen, H., Du, B., Zhang, L., 2022. Unsupervised Change Detection in Multitemporal VHR Images Based on Deep Kernel PCA Convolutional Mapping Network. *IEEE Transactions on Cybernetics*, 52(11), 12084-12098.

This contribution has been peer-reviewed.
https://doi.org/10.5194/isprs-archives-XLIX-B3-2026-643-2026 |